IMPACT MECHANICS – CASE STUDY 1:

CALIBRATION OF CONSTITUTIVE RELATIONS AND FAILURE CRITERIA FOR IMPACT PROBLEMS

Solution proposal:

1) Assuming isotropic hardening, the von Mises yield function can be defined as

$$f\left(\boldsymbol{\sigma},R,T\right)=\sigma_{eq}\left(\boldsymbol{\sigma}\right)-\left(\sigma_0\left(T\right)+R\left(p,T\right)\right) \tag{1}$$

A multiplicative constitutive relation for the strain-rate dependent material is given as

$$\dot{p}=\begin{cases}0 & \text{for} \quad f\left(\boldsymbol{\sigma},R,T\right)\le 0\\ \dot{p}_0\left(\left(\dfrac{\sigma_{eq}\left(\boldsymbol{\sigma}\right)}{\sigma_0+R\left(p\right)}\right)^{\frac{1}{C}}-1\right) & \text{for} \quad f\left(\boldsymbol{\sigma},R,T\right)>0\end{cases} \tag{2}$$

The equivalent stress, the yield stress and the hardening variable are then defined by

$$\sigma_{eq}=\sqrt{\tfrac{3}{2}\boldsymbol{\sigma}':\boldsymbol{\sigma}'} \tag{3}$$

$$\sigma_0\left(T\right)=\sigma_0\left[1-\left(T^*\right)^m\right] \tag{4}$$

$$R\left(p,T\right)=\left(\sum_{i=1}^{2}Q_{Ri}\left(1-\exp\left(-C_{Ri}p\right)\right)\right)\left[1-\left(T^*\right)^m\right] \tag{5}$$

where the homologous temperature is given as

$$T^*=\left(T-T_r\right)/\left(T_m-T_r\right) \tag{6}$$

If we now solve Equation (2) for the equivalent stress in the plastic domain, we get

$$\begin{aligned}\sigma_{eq}\left(\boldsymbol{\sigma}\right)&=\left(\sigma_0\left(T\right)+R\left(p,T\right)\right)\left(1+\frac{\dot{p}}{\dot{p}_0}\right)^C\\&=\left(\sigma_0+\sum_{i=1}^{2}Q_{Ri}\left(1-\exp\left(-C_{Ri}p\right)\right)\right)\left(1+\frac{\dot{p}}{\dot{p}_0}\right)^C\left[1-\left(T^*\right)^m\right]\end{aligned} \tag{7}$$

where the first term describes strain hardening, the second term describes strain rate hardening and the third term describes temperature softening. This shows that the MJC model fulfils the requirements of a multiplicative constitutive relation.

2) Based on the measured force and diameters from the quasi-static tension tests, the force – diameter reduction curves can be established. This is shown for test W700-QS1 in Figure 1. Only the curves from one typical test are shown since the repeatability between duplicate tests was excellent.

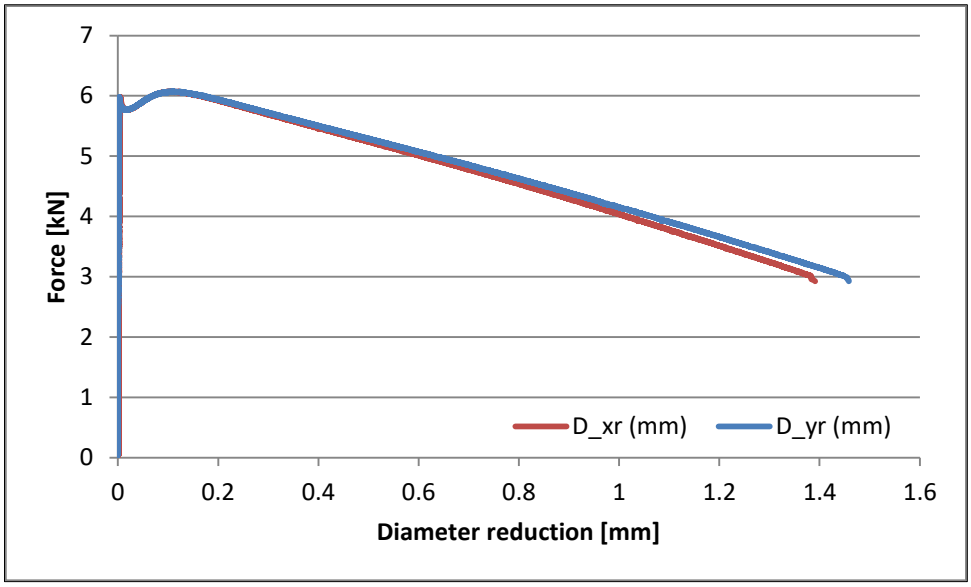

Figure 1. Force – diameter reduction curves from test W700-QS1.

The true stress and the true strain are calculated as $\sigma_t = F / A$ and $\varepsilon_l = \ln(A_0 / A)$, where $A_0 = \pi D_{x0} D_{y0} / 4$ and $A = \pi D_x D_y / 4$. Note that it has been assumed that the deformed shape of the cross-section of the specimen is an ellipse. The $\sigma_t - \varepsilon_l$ curve is plotted all the way to fracture in Figure 2.

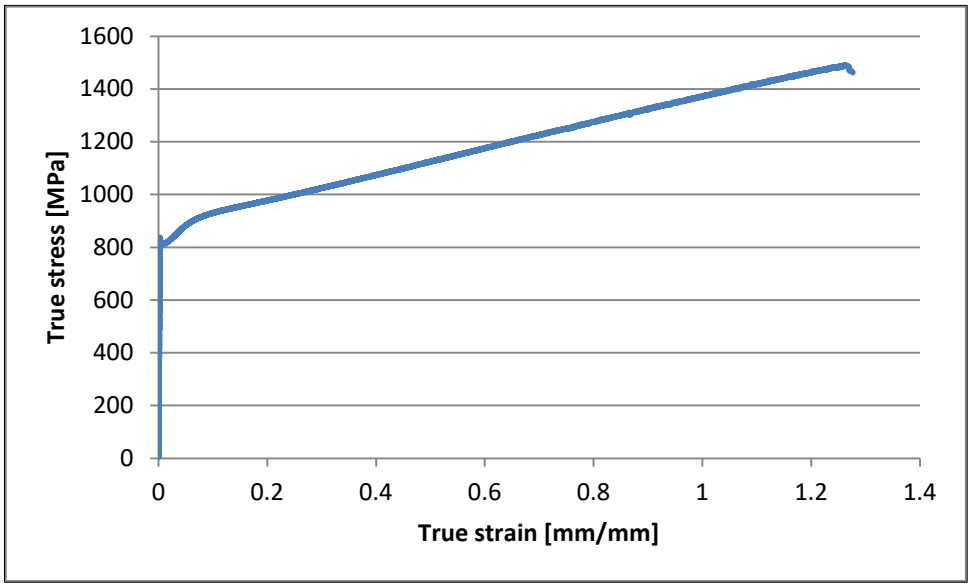

Figure 2. True stress-strain curve for test W700-QS1.

A zoom of the elastic domain in Figure 2 is shown in Figure 3. The initial stiffness is as expected too high (since no special attention was given to measure Young's modulus correctly). Young's modulus is found by linear regression to be 325000 MPa, which is rather far from the nominal value of 210000 MPa. Thus, the initial stiffness needs to be corrected. This can be done through the relation

$$\Delta\varepsilon = \varepsilon_c - \varepsilon_m \quad \Rightarrow \quad \varepsilon_c = \varepsilon_m + \Delta\varepsilon = \varepsilon_m + \left(\frac{E_m - E_c}{E_m E_c} \right) \sigma$$

where subscript c means "correct" and subscript m means "measured". A comparison between the uncorrected and the corrected stress-strain curves in the elastic domain is also given in Figure 3.

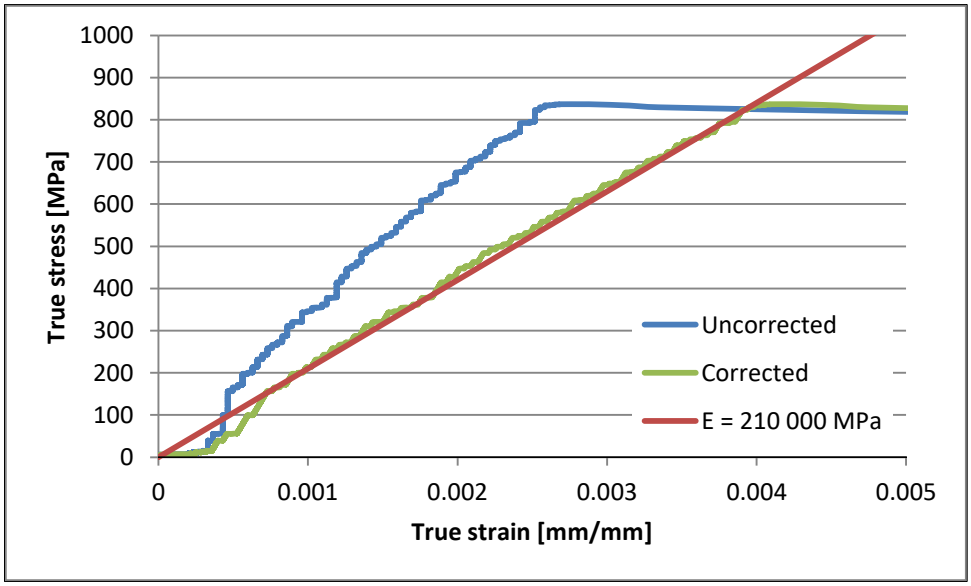

Figure 3. Correction of the initial stiffness for test W700-QS1.

Finally, from the corrected $\sigma_t - \varepsilon_l$ curve in Figure 3, the true plastic strain is found as $\varepsilon_l^p = \varepsilon_l - \sigma_t / E$. A plot of the true stress – true plastic strain curve all the way to fracture is given in Figure 4. If Figure 2 and Figure 4 are compared, it is hard to see any differences since the elastic strains are small compared to the plastic strains, but for small strains the difference is noticeable as seen in Figure 3. Keep in mind that the true stress – true plastic strain curve is always the starting point for the calibration of our constitutive relation.

Finally, as seen from Figure 1 the diameter reduction D_{xr} in the thickness direction of the plate and the diameter reduction D_{yr} in the transverse in-plane direction of the plate (and consequently the strains in these directions) are almost identical (at least up to diameter reductions > 1 mm). It is also seen that the cross-section of the failed specimen is cylindrical. Finally, we may also plot the strain ratio, defined as $R = \dot{\varepsilon}_y^p / \dot{\varepsilon}_x^p \approx \varepsilon_y^p / \varepsilon_x^p$, to check that it is equal to unity. All this gives an indication that the material for practical applications can be considered as isotropic. However, to really confirm that the material is isotropic, we have to confirm material tests in different material directions and compare the results.

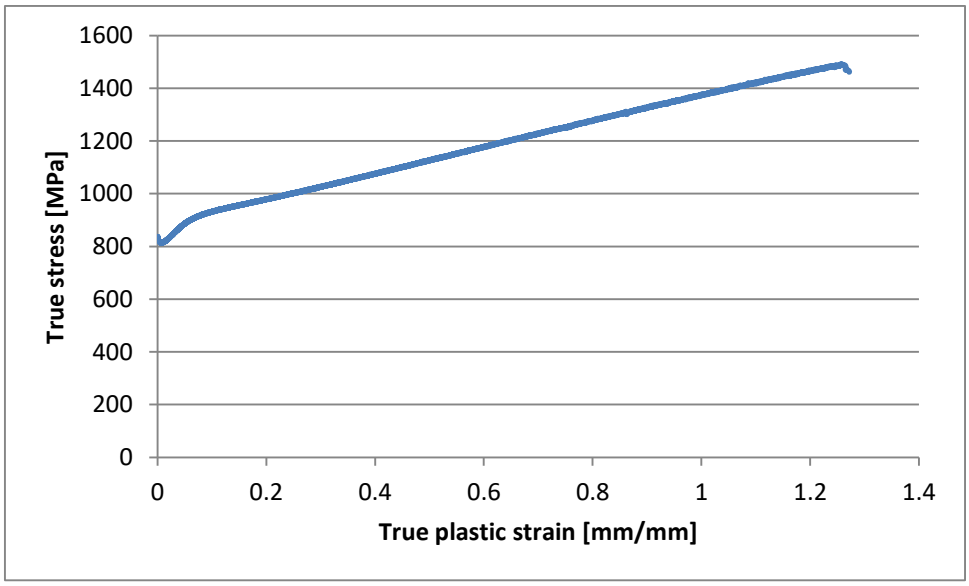

Figure 4. True stress – true plastic strain curve for test W700-QS1.

3) Next, the formation of a neck in the tensile specimen introduces a complex triaxial stress state giving radial and transverse stresses which raise the value of the longitudinal stress required to cause plastic flow. In other words, the measured true stress needs to be corrected for triaxiality effects, since this stress is not equal to the equivalent stress after necking. The equivalent stress after necking can be obtained using the Bridgman-LeRoy correction given as

$$\sigma_{eq} = \frac{\sigma_t}{\left(1+2R/a\right)\ln\left(1+a/2R\right)}$$

where

$$a/R = 1.1\left(\varepsilon_{eq} - \varepsilon_{lu}^{p}\right)$$

In order to use this correction, we have to determine the true plastic strain ε_{lu}^{p} at necking. To do this it is possible to use Considère's criterion, but without smooth functions the derivation becomes messy. However, necking occurs at maximum load, i.e., when $dF = 0$. From the spreadsheet $F_{\max}$ is found to be 6.075 kN and the corresponding value for ε_{lu}^{p} is 0.08. The Bridgman-corrected $\sigma_{eq} - \varepsilon_{eq}$ curve to failure is compared with the $\sigma_t - \varepsilon_l^p$ curve in Figure 5. Remember that in the uniaxial tension test $\sigma_t = \sigma_{eq}$ before necking, and that $\varepsilon_l^p = p$. The failure strain is defined as the strain at maximum true stress. From the spreadsheet we find $\sigma_{\max} = \sigma_f = 1491$ MPa and a corresponding failure strain $\varepsilon_f = 1.26$ or 126%. Note the large difference in necking strain and failure strain (8% versus 126%). In "standard" tensile tests the extensometer is removed at necking, and the stress-strain curve after maximum loading is based on extrapolation. This may cause large errors at large strains. Some material data from test W700-QS1 is given in Table 1. Here the yield stress σ_0 is taken as the true stress at zero plastic strain, while σ_u is the true stress at necking.

Table 1: Some material data from test W700-QS1.

σ_0 (MPa)	σ_u (MPa)	ε_{lu}^p (-)	σ_f (MPa)	ε_f (-)
833.5	849	0.08	1491	1.26

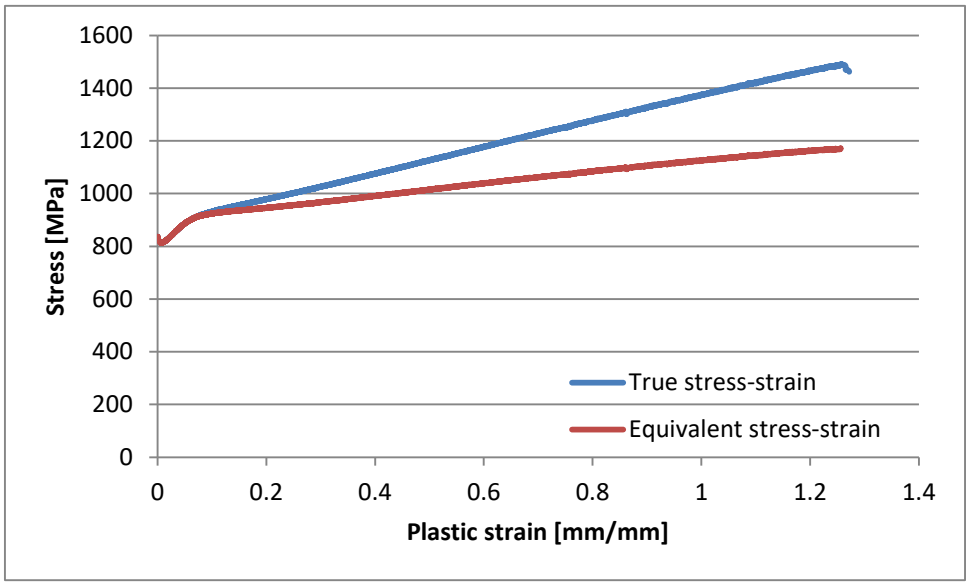

Figure 5. Comparison between true stress – plastic strain curve and Bridgman-corrected equivalent stress – plastic strain curve for test W700-QS1.

4) MS Excel (using the solver function and the method of least squares) is used to fit the material parameters in the constitutive relations (JC or MJC) to the Bridgman-corrected $\sigma_{eq} - p$ curve, assuming that $\dot{p}^* \approx 1$ and $T^* = 0$. This means that the strain rate term in the MJC constitutive relation is $\left(1 + \dot{p}^*\right)^C = 2^C$. However, since C is small for most metallic materials, it is reasonable to assume that $2^C \approx 1$. A comparison between the fitted constitutive relations and the measured $\sigma_{eq} - p$ curve is given in Figure 6. The agreement between the model fits and the test data is as seen good, even though no special attention has been paid in order to capture the yield point and plateau (everything is just based on a best possible fit).

Regarding fracture, we do not have sufficient material data to calibrate the JC fracture criterion in this case study. These data are therefore taken from the literature. For the CL fracture criterion, the critical constant is given as $W_C = \int_0^{\varepsilon_f} \sigma_t d\varepsilon_l^p$. Thus, the true stress-plastic strain curve as shown in Figure 5 (without Bridgman corrections) is used to find the critical CL constant by numerical integration, and a value of 1492 MPa is obtained. The temperature sensitivity constant m is taken equal to unity for both models.

Fitted material constants for the JC model are given in Table 2, while fitted material constants for the MJC model are given in Table 3. Physical constants required for numerical simulations are taken from the literature, and can be found in Table 4.

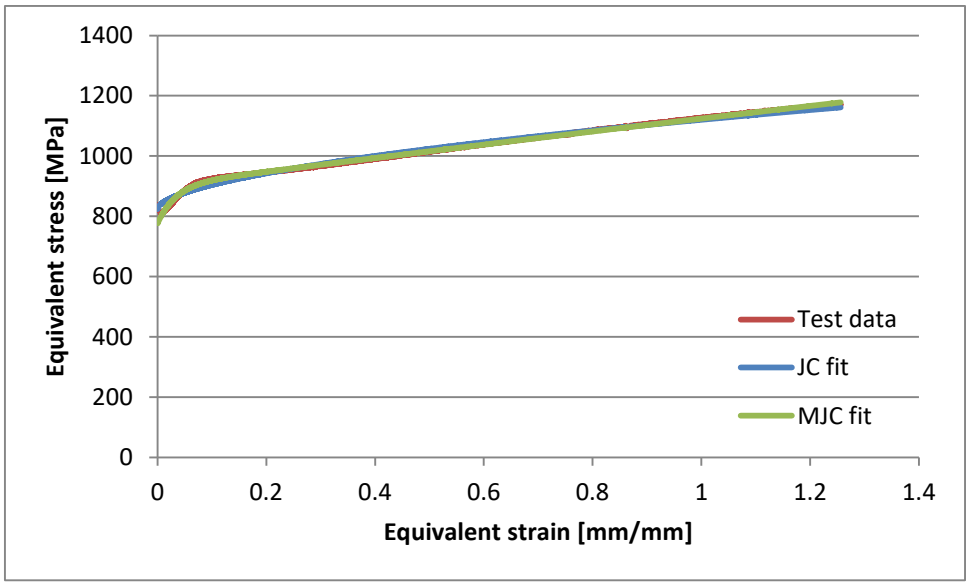

Figure 6. Comparison between test data, JC fit and MJC fit for test W700-QS1.

Table 2: Fitted material constants – JC.

A (MPa)	B (MPa)	n (-)	C (-)	m (-)	D_1 (-)	D_2 (-)	D_3 (-)	D_4 (-)	D_5 (-)
824.6	295.6	0.57	0.01	1.0	0.361	4.768	5.107	-0.0013	1.333

Table 3: Fitted material constants – MJC.

σ_0 (MPa)	Q_{R1} (MPa)	C_{R1} (-)	Q_{R2} (MPa)	C_{R2} (-)	C (-)	m (-)	W_C (MPa)
777.0	125.2	29.5	2670.5	0.09	0.01	1.0	1492

Table 4: Physical constants and model parameters.

E (MPa)	ν (-)	ρ (kg/m^3)	$\dot{p}_0$ (s^{-1})	c_ε (J/kg K)	T_0 (K)	T_m (K)	β (-)
210000	0.33	7850	$5 \cdot 10^{-4}$	452	293	1800	0.9

5) The 2D axisymmetric element model used in Abaqus is shown in Figure 7. The same model was applied in both implicit and explicit simulations. 17 elements were used over the cross-section radius of the specimen, giving an element size of 0.15×0.08 mm^2 in the gauge area. The axisymmetric element CAX4R is used in all simulations. These elements are using a reduced integration scheme and the potential hourglass modes are compensated using the default algorithm in Abaqus. During quasi-static testing, the specimen was fixed at the right-hand side and pulled by a displacement (up to 3 mm) at the left-hand side in the implicit simulation, while in the explicit simulation a velocity of 5 m/s was used. It was checked that the applied time scaling did not introduce any dynamic effects into the problem. The velocity was ramped onto the specimen using a smooth function to avoid oscillations in the results, and the ramping time was 10% of the total simulation time. Both the JC and the MJC models were investigated, using the material data provided in Table 2, Table 3 and Table 4 with $C = 0$ and $\beta = 0$. Fracture was only considered in the explicit simulations.

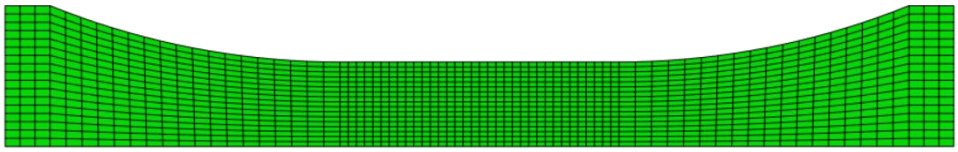

Figure 7. Abaqus-model used in FE simulations.

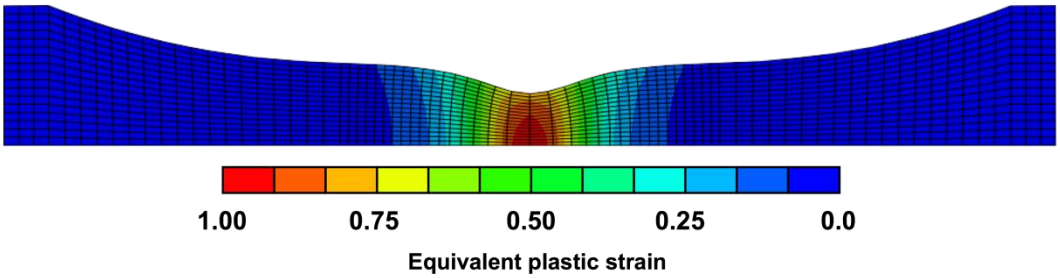

Figure 8. Necking in the specimen using the MJC model and the explicit solver of Abaqus.

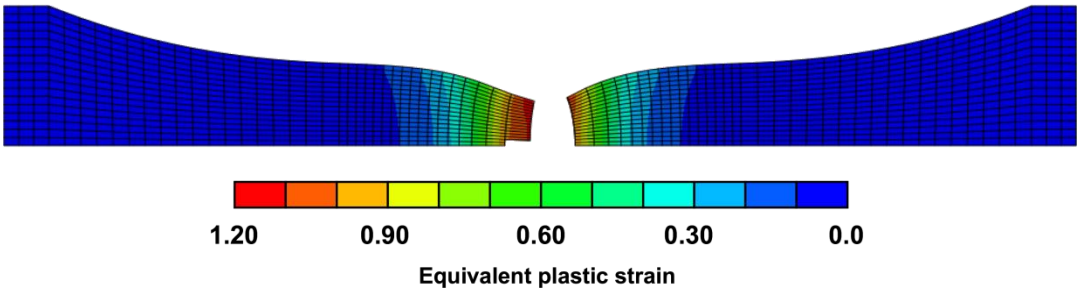

Figure 9. Fracture in the specimen using the MJC model and the explicit solver of Abaqus.

Figure 8 shows the necking in the specimen from one of the simulations, while Figure 9 shows the final fracture. It is seen that both the neck and the fracture are well captured by the model, and that the strain field is heterogeneous over the cross-section (with highest plastic strain close to the centre of the specimen where failure is assumed to initiate).

Comparisons of force – diameter reduction curves from the test and the JC and the MJC models are given in Figure 10 and Figure 11, respectively. The overall agreements are as seen good, but it is quite clear from Figure 10 that the JC model predicts fracture too early in the specimen. The MJC model, on the other hand, predicts also fracture well. In order to improve the results using the JC fracture criteria, inverse modelling of the fracture constants given in Table 2 may be required. Hardly any differences are found between the implicit and the explicit simulations. However, fracture is not considered in the former.

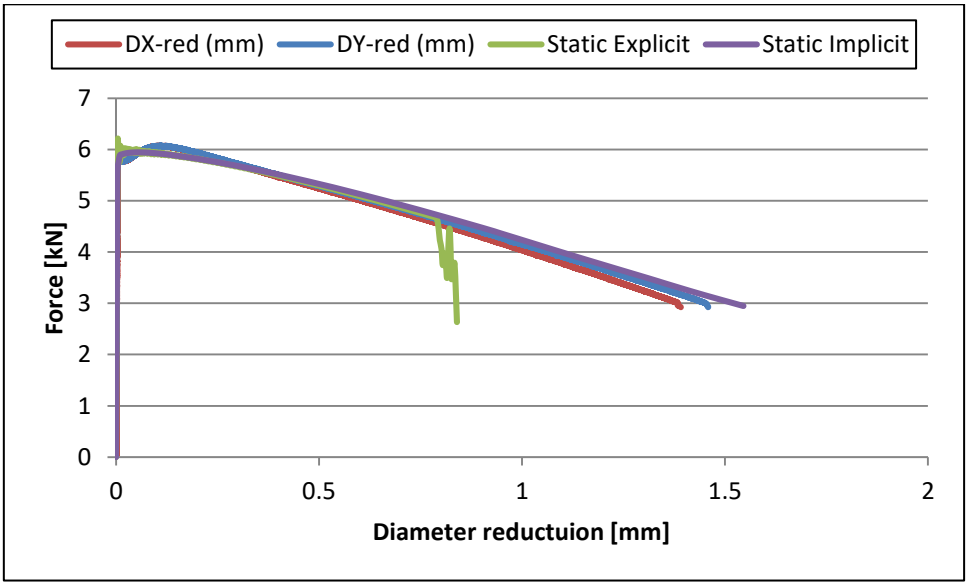

Figure 10. Comparison of force – diameter reduction curves from the test and the JC model.

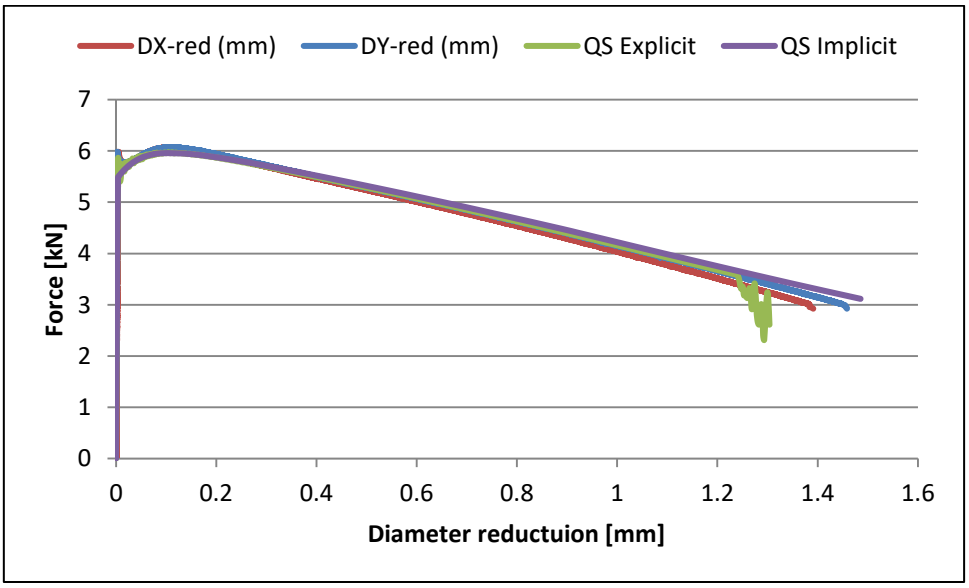

Figure 11. Comparison of force – diameter reduction curves from the test and the MJC model.

6) Figure 12 shows the stress-strain curves from the SHTB-tests at elevated strain rates. Compared with the stress-strain curves from the quasi-static tests (see e.g. Figure 2) the material is clearly strain-rate sensitive. Following the same procedures as used in previous tasks (i.e., correction of the elastic stiffness, calculation of the $\sigma_t - \varepsilon_l$ curve and finally the $\sigma_t - \varepsilon_l^p$ curve), the true stress – plastic strain curve shown in Figure 13 can be constructed. Note that only data in the pre-necking phase should be used in the calibration of the strain-rate sensitivity constant (i.e. no Bridgman correction), and that $\sigma_{eq} = \sigma_t$ and $p = \varepsilon_l^p$ before necking in the uniaxial tension test. Based on these curves, the true stress for different values of the true plastic strain and strain rate is collected in Table 5 and plotted in Figure 14. Also results from the quasi-static test are included.

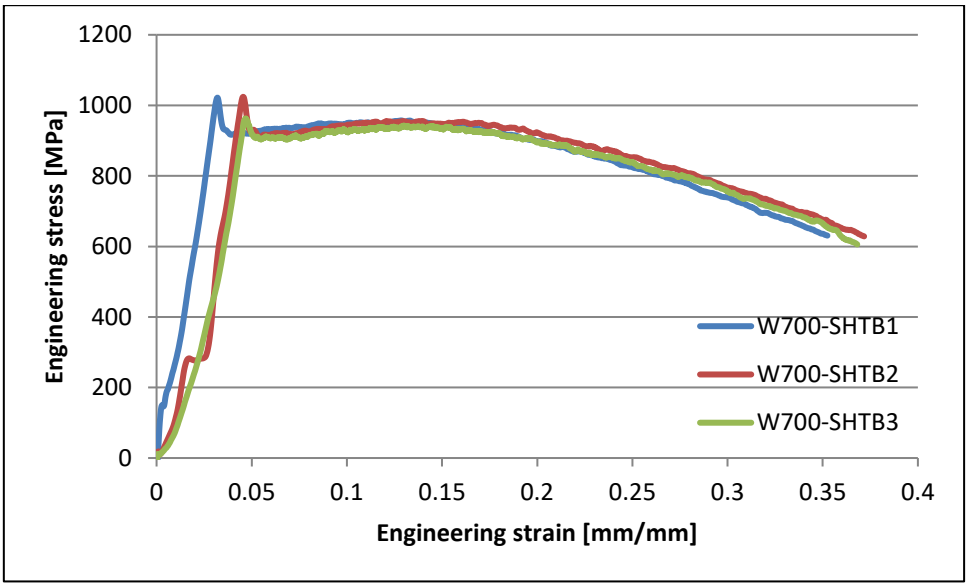

Figure 12. Engineering stress – strain curves from SHTB-tests at elevated strain rates.

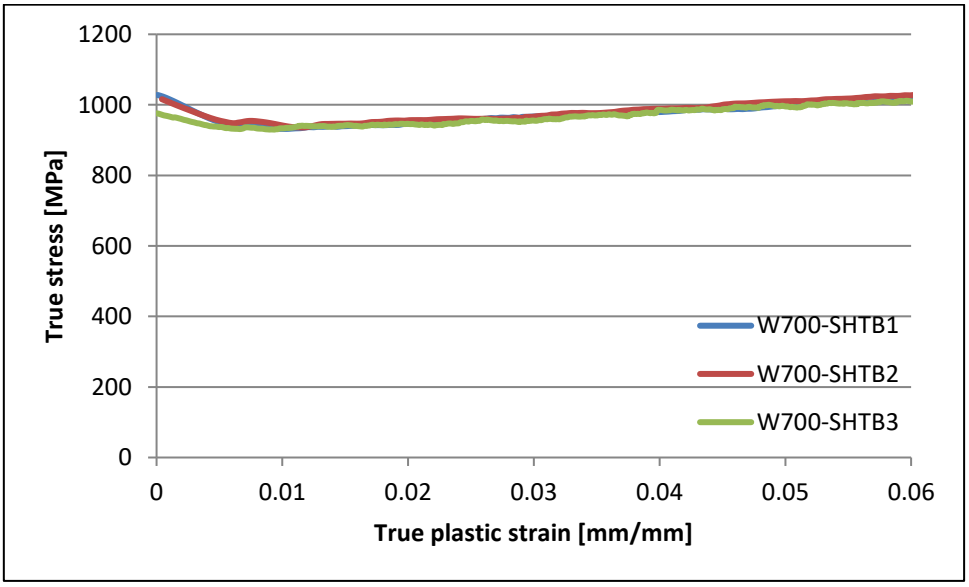

Figure 13. True stress – plastic strain curves from SHTB-tests at elevated strain rates.

Table 5: True stresses for different values of true plastic strain and strain rate in the pre-necking phase from one quasi-static test and the SHTB tests.

Test #	$\sigma_t\left(p=2\%\right)$	$\dot{p}$ (s^{-1})	$\sigma_t\left(p=4\%\right)$	$\dot{p}$ (s^{-1})	$\sigma_t\left(p=6\%\right)$	$\dot{p}$ (s^{-1})
W700- QS1	830.0	$5\cdot10^{-4}$	869.8	$5\cdot10^{-4}$	900.1	$5\cdot10^{-4}$
W700-SHTB1	946.1	139	985.5	102	1008.9	104
W700- SHTB2	946.2	364	979.5	357	1012.6	346
W700- SHTB3	956.4	443	988.9	423	1026.9	400

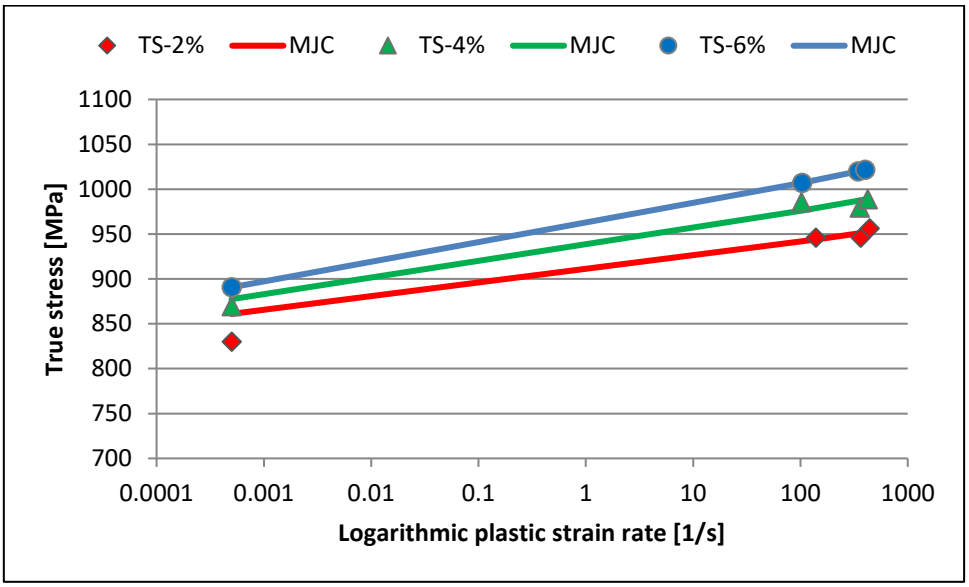

Figure 14. True stress – logarithmic plastic strain data from one quasi-static test and SHTB-tests at elevated strain rates compared to the MJC model.

Based on fits to the experimental data using the method of least squares (here using the solver function in MS Excel), the strain-rate sensitivity constant C in both the JC model and the MJC model is obtained for $T^*=0$ (i.e. room temperature). It is thus provided that the possible temperature increase due to adiabatic heating during the dynamic tests is negligible. The material constants for the strain hardening are already known, and given in Table 2 and Table 3. Note that C is first fitted for each constant value of the plastic strain, and then the average value, $C_{avg}=\left(C(p=2\%)+C(p=4\%)+C(p=6\%)\right)/3$, is used in the subsequent simulations. From this a strain-rate sensitivity constant C of about 0.01 was found for both constitutive relations.

7) Finally, the same 2D axisymmetric element model of the material test specimen as used in Task 5) was used in dynamic (explicit) simulations. The only differences compared with the quasi-static (explicit) simulations were that the strain-rate sensitivity constant C was applied in the material card (the loading rate was similar since time scaling was used in the explicit quasi-static simulations). In addition, both isothermal and adiabatic simulations were run using β equal to 0 and 0.9, respectively. Dynamic force-diameter reduction curves for both constitutive relations are compared with corresponding quasi-static curves in Figure 15 and Figure 16, respectively. Only the dynamic results for the adiabatic simulations are shown,

since they seemed to give the best results. As seen, the strain-rate sensitivity effect of an increased force (or stress) at the same diameter reduction (strain) is well captured, while the failure strain is hardly affected. Thus, the strain-rate sensitivity of the material is clearly described.

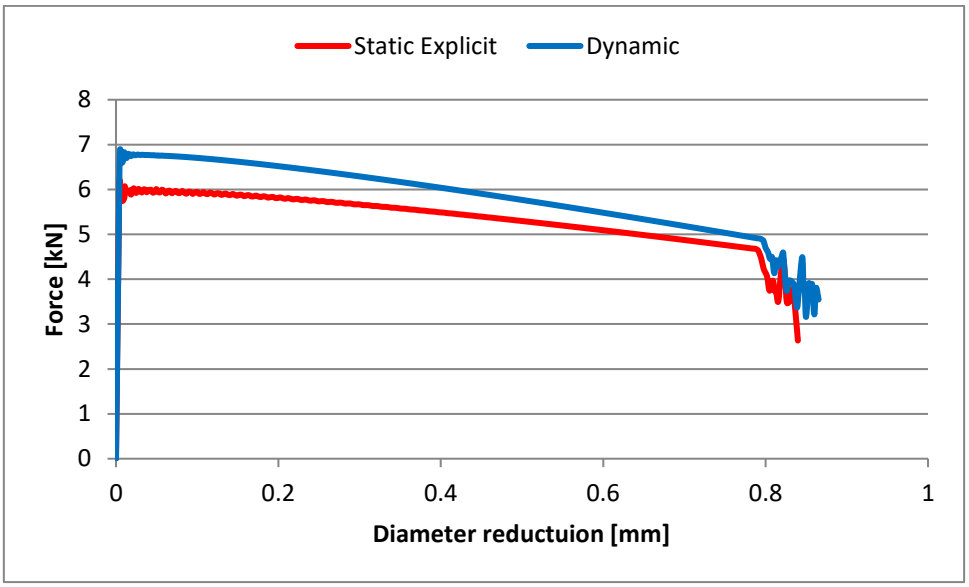

Figure 15. Comparison between quasi-static and dynamic results using the JC model.

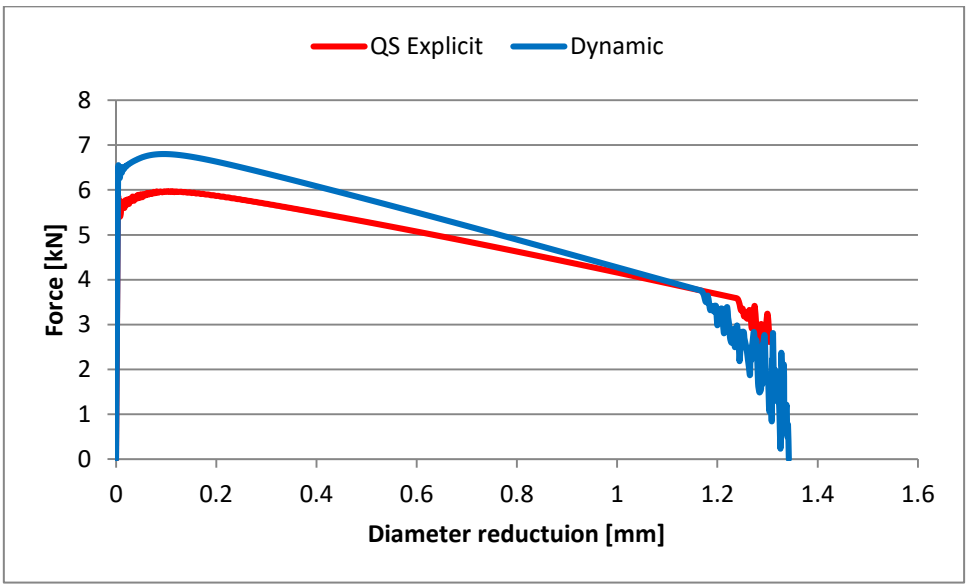

Figure 16. Comparison between quasi-static and dynamic results using the MJC model.